A

B

C

D Non-insertion/deletion   insertion/deletion
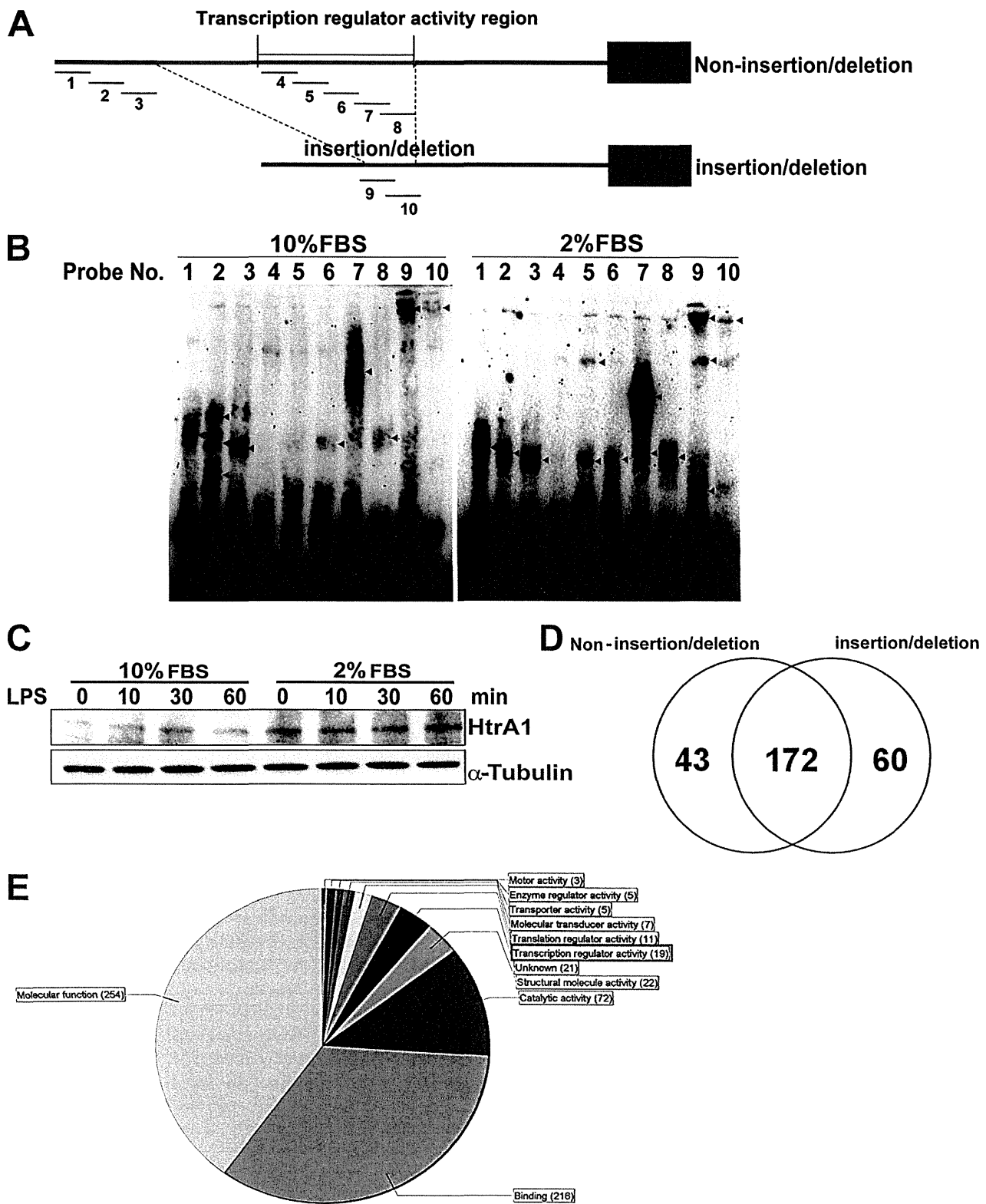

E

FIGURE 6. **Identification of the transcription factors binding to non-insertion/deletion and insertion/deletion regions of the *HTRA1* transcription regulators.** *A*, location of the double-stranded DNA probes, *1–10*, in the region upstream of the *HTRA1* coding region that were designed for EMSAs. Both non-insertion/deletion and insertion/deletion *HTRA1* transcription regulatory regions were targeted. *B*, EMSAs of probes 1–10 using nuclear extracts from 661W cells cultured in 2 and 10% FBS. *Red arrowheads*, detected signals. *C*, increased expression of HtrA1 was detected in Western blot assays performed following treatment of 661W cells with LPS (1 μg/ml, 0–60 min) using anti-mouse HtrA1 antibodies. Detection of α-tubulin was used as an internal control. *D*, a Venn diagram shows the number of proteins found to bind the non-insertion/deletion *versus* insertion/deletion regions of the *HTRA1* transcription regulator based on LC-MS/MS data. *E*, gene ontology term of non-insertion/deletion- and insertion/deletion-binding protein (categorized by molecular function).

35

iPSCs heterozygous and homozygous for the insertion/deletion type regulatory element sequence were subjected to genotyping. From both control and AMD patients, iPSCs were collected and categorized as having a non-insertion/deletion or insertion/deletion genotype (Fig. 5A). These cells were also assayed for expression of the iPSCs markers, OCT3/4, NANOG, and SOX2 (Fig. 5B), and levels of *HTRA1* mRNA were measured by RT-PCR and quantitative RT-PCR (Fig. 5, B and C). Individuals with heterozygous or homozygous *HTRA1* insertion/deletion type sequences showed an approximately 6- and 7-fold increase in *HTRA1* mRNA levels, respectively, compared with individuals having the non-insertion/deletion type sequence (Fig. 5C). In contrast, expression of *HTRA1* mRNA was not influenced by the heterozygous or homozygous state of the insertion/deletion type sequence.

Analysis of Regulatory Element-binding Proteins—To detect proteins that bind the *HTRA1* regulatory element, EMSAs were performed. Ten 3'-biotin-labeled double-stranded DNA probes were generated in order to assay the transcriptional activity of each region of the *HTRA1* regulatory element (Figs. 4 (B and C) and 6A and Table 3). In addition to the use of 661W nuclear extracts in these assays, extracts of 661W cells grown in 10% FBS *versus* 2% FBS were also assayed; the latter conditions were included based on the observation that HTRA1 family proteins are known to mediate various stress response signaling pathways (25–28). Thus, we tested 661W cell protein-probe binding activity in a cell-stressful environment. Protein-probe binding signals were detected for probes 1–3 and 6–10 (Fig. 6A) in the presence of nuclear extracts from normally cultured 661W cells (Fig. 6B, *left*). These results suggest that the binding pattern of the insertion/deletion sequence (included in probes 4–8) may differ greatly from that of the non-insertion/deletion type sequence (number 9 and 10 probes). When the culturing conditions for the 661W cells were changed from 10% to 2% FBS, this drastically altered the protein-probe binding signal pattern obtained (Fig. 6B, *right*). For example, a reduction in FBS concentration resulted in the loss of two of three signals for the number 2 probe, and it altered the probe-protein binding pattern of probes 5–9. Detection of HtrA1 expression further demonstrated that HtrA1 expression was enhanced in 661W cells following starvation stress (Fig. 6C). Signaling pathways involving the Toll-like receptor (TLR) family of proteins have been shown to be associated with AMD pathogenesis (29), and 661W cells are known to express TLR-4 (30). Therefore, HtrA1 expression was assayed in 661W cells following stimulation with a TLR-4 ligand, lipopolysaccharide (LPS). However, HtrA1 expression was unaffected by this stimulation (Fig. 6C).

To identify the proteins that bind the regulatory element region of *HTRA1*, both non-insertion/deletion and insertion/deletion sequence-binding factors were analyzed by LC-MS/MS. Non-insertion/deletion-binding protein samples were incubated with probes 4–8, whereas the insertion/deletion-binding protein samples were incubated with probes 9 and 10 (Fig. 6A). A total of 172 common binding proteins, 43 non-insertion/deletion probe-specific binding proteins, and 60 insertion/deletion probe-specific binding proteins were identified (Fig. 6D). Using Scaffold 4 software, 19 transcriptional regulator proteins were detected (according to gene ontology (see

the Gene Ontology Consortium Web site)) (Fig. 6E). These 19 factors were then classified according to their binding sequence (Tables 4–6). Six non-insertion/deletion-binding probes were found to bind PURB, NFIC, RUNX2, PEBB, APEX1, and RBM14 proteins (Table 4), whereas three insertion/deletion-binding probes were found to bind LYRIC (lysine-rich CEACAM1 co-isolated) protein, MED4, and PHF2 (Table 5). Ten additional proteins were found to bind both the non-insertion/deletion and insertion/deletion probes: ROAA, SHOX2, CUX1, DDX5, DDX1, MED24, RBM39, JMY, TCP4, and DDX17 (Table 6). In combination, these results suggest that expression of *HtrA1* is influenced by factors that specifically bind this region and affect gene expression.

DISCUSSION

To the best of our knowledge, the present study provides the first detailed characterization of regulatory elements for *HTRA1* and the effect of insertion/deletion sequences associated with wet AMD. The insertion/deletion variant that exhibited complete association with the SNP, rs10490924, is the only major sequence change in this LD block and is likely to play a major role in disease onset. Moreover, the insertion/deletion variant in close proximity to *ARMS2* and *HTRA1* has been at the center of the discussion of whether one or both genes are involved in AMD (19, 24). In the present study, the *ARMS2* transcription regulator exhibited only marginal activity in each of the cell lines tested, whereas robust up-regulation of *HTRA1* transcription regulator activity was observed in iPSCs derived from AMD patients containing heterozygous or homozygous forms of the insertion/deletion. Up-regulation of *HTRA1* in the earliest stages of development is predicted to affect the entire body (31).

HTRA1 is known to be a TGF-β suppression factor, and some reports have suggested that HtrA1 is expressed in skeletal, brain, lung epithelium, heart, and skin tissues in fetal mice (31). Other reports have suggested that HTRA1 is involved in bone remodeling (*e.g.* RANK/RANKL signal-derived osteoclast bone absorption and osteoblast differentiation) (32) and oncogenesis in liver and lung cancers (33, 34). Thus, HTRA1 may play an important role in cell growth and differentiation, tissue and/or organ formation, and the onset of disorders. Correspondingly, a transgenic mouse with expression of mouse *HtrA1* driven by a chicken actin (CAG) promoter was used to establish a model for choroidal neovascularization, and this model exhibited a significant reduction in tolerance to smoking (23).

Detailed characterization of the transcription regulator activity that surrounds the *HTRA1* insertion/deletion sequence showed that suppressive regions are located between bp −4,320 and −4,239 and between bp −3,936 and −3,778 in the non-insertion/deletion sequence and between bp −3,936 and −3,854 for the insertion/deletion sequence. In addition, the insertion/deletion located between bp −3,836 and −3,783 exhibited transcription regulator activity unique to the insertion/deletion sequence (Fig. 4). An analysis of these results showed that the insertion/deletion variant interrupts a suppressor *cis*-element and replaces it with an activator, and this significantly alters *HTRA1* transcription in the photoreceptor.

36

TABLE 4

Non-insertion/deletion probe binding proteins

MS/MS view: identified proteins	Symbol	Molecular mass	Taxonomy	Biological regulation	Binding	Molecular function	Transcription regulator activity	Peptide hit score (non-indel)[a]	Peptide Hit Score (indel)
		kDa							
Transcriptional activator protein Pur-β	PURB	34	M. musculus	Regulation of transcription, DNA-dependent	Protein binding	Transcription factor activity	Transcription factor activity	3	0
Nuclear factor 1 C-type	NFIC	49	M. musculus	Regulation of transcription, DNA-dependent	Transcription factor activity	Transcription factor activity	Transcription factor activity	3	0
Runt-related transcription factor 2	RUNX2	66	M. musculus	Positive regulation of transcription from RNA polymerase II promoter	Protein binding	Transcription factor activity	Transcription factor activity	2	0
Core-binding factor subunit β	PEBB	22	M. musculus	Positive regulation of transcription from RNA polymerase II promoter	DNA binding	Transcription coactivator activity	Transcription coactivator activity	1	0
DNA-(apurinic or apyrimidinic site) lyase	APEX1	35	M. musculus	Cell redox homeostasis	Chromatin DNA binding	Transcription coactivator activity	Transcription coactivator activity	1	0
RNA-binding protein 14	RBM14	69	M. musculus	Regulation of transcription, DNA-dependent	Nucleic acid binding	Ligand-dependent nuclear receptor transcription coactivator activity	Ligand-dependent nuclear receptor transcription coactivator activity	1	0

[a] indel, insertion/deletion.

TABLE 5

Insertion/deletion probe binding proteins

MS/MS view: identified proteins	Symbol	Molecular mass	Taxonomy	Biological regulation	Binding	Molecular function	Transcription Regulator Activity	Peptide Hit Score (non-indel)[a]	Peptide Hit Score (indel)
		kDa							
Protein LYRIC	LYRIC	64	M. musculus	Positive regulation of NF-κB transcription factor activity	Nucleolus	Protein binding	Transcription coactivator activity	0	20
Mediator of RNA polymerase II transcription subunit 4	MED4	30	M. musculus	Androgen receptor signaling pathway	Thyroid hormone receptor binding	Transcription cofactor activity	Transcription cofactor activity	0	2
Lysine-specific demethylase PHF2	PHF2	121	M. musculus	Regulation of transcription, DNA-dependent	Methylated histone residue binding	Transcription coactivator activity	Transcription coactivator activity	0	1

[a] indel, insertion/deletion.

TABLE 6
Non-insertion/deletion-probe and insertion/deletion probe-binding proteins

MS/MS view: identified proteins	Symbol	Molecular mass (kDa)	Taxonomy	Biological regulation	Binding	Molecular Function	Transcription Regulator Activity	Peptide hit score (non-indel)[a]	Peptide hit score (indel)
Heterogeneous nuclear ribonucleoprotein A/B	HNRPAB	31	M. musculus	Regulation of transcription, DNA-dependent	Nucleic acid binding	Transcription factor activity	Transcription factor activity	25	24
Short stature homeobox protein 2	SHOX2	35	M. musculus	Positive regulation of transcription from RNA polymerase II promoter	DNA binding	Transcription factor activity	Transcription factor activity	2	1
Homeobox protein cut-like 1	CUX1	166	M. musculus	Negative regulation of transcription from RNA polymerase II promoter	Chromatin binding	Transcription factor activity	Transcription factor activity	6	1
Probable ATP-dependent RNA helicase DDX5	DDX5	69	M. musculus	Regulation of alternative nuclear mRNA splicing, via spliceosome	Nucleic acid binding	Transcription coactivator activity	Transcription cofactor activity	14	36
ATP-dependent RNA helicase DDX1	DDX1	83	M. musculus	Regulation of transcription, DNA-dependent	Chromatin binding	Transcription cofactor activity	Transcription cofactor activity	28	12
Mediator of RNA polymerase II transcription subunit 24	MED24	110	M. musculus	Stem cell maintenance	Thyroid hormone receptor binding	Receptor activity	Transcription cofactor activity	1	1
RNA-binding protein 39	RBM39	59	M. musculus	Regulation of transcription, DNA-dependent	Nucleic acid binding	Transcription coactivator activity	Transcription coactivator activity	10	9
Junction-mediating and -regulatory protein	JMY	111	M. musculus	Positive regulation of transcription factor activity	Protein binding	Transcription coactivator activity	Transcription coactivator activity	1	1
Activated RNA polymerase II transcriptional coactivator p15	TCP4	14	M. musculus	Regulation of transcription from RNA polymerase II promoter	DNA binding	Transcription coactivator activity	Transcription coactivator activity	1	2
Probable ATP-dependent RNA helicase DDX17	DDX17	72	M. musculus	Regulation of transcription, DNA-dependent	Nucleic acid binding	Hydrolase activity	Transcription coactivator activity	1	1

[a] indel, insertion/deletion.

Characterization of HTRA1 Regulatory Elements

The EMSA and LC-MS/MS data also suggest that *HTRA1* regulatory element activity is regulated by a number of transcription factors (Fig. 6 and Tables 4–6).

When the proteins that bound the regulatory elements of the non-insertion/deletion and insertion/deletion sequences of *HTRA1* were analyzed using LC-MS/MS, LYRIC (also known as MTDH/AEG1) was a high hit score insertion/deletion-binding protein that was identified (Table 5). LYRIC is known to promote hepatocellular carcinoma and to activate the transcription factor, nuclear factor κ-B (NF-κB), and also has an effect on bone and brain metastasis (35–37). Regarding the latter, LYRIC may enhance the seeding of tumor cells at the target organ endothelium. LYRIC also contributes to HIF-1α-mediated angiogenesis (38), with HIF-1α playing an important role in the activation of VEGF signaling in response to oxidative stress (39). Recently, Oka *et al.* (25) reported that *HTRA1* gene expression is enhanced by oxidative stress. This result is consistent with the observation that AMD onset is associated with a variety of stresses, and stress response factors may play an important role.

Both common sequences (non-insertion/deletion (bp −4,320 to −4,220) and insertion/deletion (bp −3,936 to −3,836 bp)) and the insertion/deletion sequence (bp −3,836 to −3,782 bp) are partially associated with *ARMS2* exon 2, thereby indicating that this exon represents a protein-coding region and a *HTRA1* regulatory element region. Recent reports have suggested that both an increase in HTRA1 transcription and a decrease in ARMS2 transcription confer an increased risk of AMD (8). These insights suggest that *ARMS2* gene expression may be regulated by *HTRA1* transcription regulator activity via the *ARMS2* exon 2 region.

AMD pathogenesis and previous *HTRA1* experiments related to AMD have been performed and discussed in relation to the RPE (8, 16, 17). However, immunostaining of *HTRA1* in mouse retinas in the present study showed that the majority of transcription occurs in the photoreceptor cell layer (Fig. 3). This result was confirmed when higher levels of transcription from the *HTRA1* insertion/deletion regulator were observed in the photoreceptor cell line: 661W cells *versus* the RPE cells (Fig. 1, *I–K*). Photoreceptors are densely concentrated in the macula (40), which predicts that HTRA1 will also be concentrated in the macula. A recent report using transgenic mice overexpressing human HTRA1 in the RPE showed that PCV-like capillary structures could be observed in the choroid. Vierkotten *et al.* (17) also observed fragmentation of the elastic layer in Bruch's membrane, and Jones *et al.* (16) reported branching of choroidal vessels, polypoidal lesions, and severe degeneration of the elastic lamina or tunica media of choroidal vessels in the same model. When HtrA1 expression was driven by the CAG promoter in a transgenic mouse model, an even more severe phenotype was induced compared with previous reports of AMD patient-like choroidal neovascularization (23). These results indicate that overexpression of HtrA1 alone can evoke choroidal vasculopathy or neovascularization, and they also provide supporting evidence for the association of the insertion/deletion variant of *HTRA1* regulatory element with wet AMD (7, 8).

38

REFERENCES

1. Fritsche, L. G., Chen, W., Schu, M., Yaspan, B. L., Yu, Y., Thorleifsson, G., Zack, D. J., Arakawa, S., Cipriani, V., Ripke, S., Igo, R. P., Jr., Buitendijk, G. H., Sim, X., Weeks, D. E., Guymer, R. H., Merriam, J. E., Francis, P. J., Hannum, G., Agarwal, A., Armbrecht, A. M., Audo, I., Aung, T., Barile, G. R., Benchaboune, M., Bird, A. C., Bishop, P. N., Branham, K. E., Brooks, M., Brucker, A. J., Cade, W. H., Cain, M. S., Campochiaro, P. A., Chan, C. C., Cheng, C. Y., Chew, E. Y., Chin, K. A., Chowers, I., Clayton, D. G., Cojocaru, R., Conley, Y. P., Cornes, B. K., Daly, M. J., Dhillon, B., Edwards, A. O., Evangelou, E., Fagerness, J., Ferreyra, H. A., Friedman, J. S., Geirsdottir, A., George, R. J., Gieger, C., Gupta, N., Hagstrom, S. A., Harding, S. P., Haritoglou, C., Heckenlively, J. R., Holz, F. G., Hughes, G., Ioannidis, J. P., Ishibashi, T., Joseph, P., Jun, G., Kamatani, Y., Katsanis, N., C, N. K., Khan, J. C., Kim, I. K., Kiyohara, Y., Klein, B. E., Klein, R., Kovach, J. L., Kozak, I., Lee, C. J., Lee, K. E., Lichtner, P., Lotery, A. J., Meitinger, T., Mitchell, P., Mohand-Said, S., Moore, A. T., Morgan, D. J., Morrison, M. A., Myers, C. E., Naj, A. C., Nakamura, Y., Okada, Y., Orlin, A., Ortube, M. C., Othman, M. I., Pappas, C., Park, K. H., Pauer, G. J., Peachey, N. S., Poch, O., Priya, R. R., Reynolds, R., Richardson, A. J., Ripp, R., Rudolph, G., Ryu, E., Sahel, J. A., Schaumberg, D. A., Scholl, H. P., Schwartz, S. G., Scott, W. K., Shahid, H., Sigurdsson, H., Silvestri, G., Sivakumaran, T. A., Smith, R. T., Sobrin, L., Souied, E. H., Stambolian, D. E., Stefansson, H., Sturgill-Short, G. M., Takahashi, A., Tosakulwong, N., Truitt, B. J., Tsironi, E. E., Uitterlinden, A. G., van Duijn, C. M., Vijaya, L., Vingerling, J. R., Vithana, E. N., Webster, A. R., Wichmann, H. E., Winkler, T. W., Wong, T. Y., Wright, A. F., Zelenika, D., Zhang, M., Zhao, L., Zhang, K., Klein, M. L., Hageman, G. S., Lathrop, G. M., Stefansson, K., Allikmets, R., Baird, P. N., Gorin, M. B., Wang, J. J., Klaver, C. C., Seddon, J. M., Pericak-Vance, M. A., Iyengar, S. K., Yates, J. R., Swaroop, A., Weber, B. H., Kubo, M., Deangelis, M. M., Leveillard, T., Thorsteinsdottir, U., Haines, J. L., Farrer, L. A., Heid, I. M., and Abecasis, G. R. (2013) Seven new loci associated with age-related macular degeneration. *Nat. Genet.* 10.1038/ng.2578

2. Klein, R. J., Zeiss, C., Chew, E. Y., Tsai, J. Y., Sackler, R. S., Haynes, C., Henning, A. K., SanGiovanni, J. P., Mane, S. M., Mayne, S. T., Bracken, M. B., Ferris, F. L., Ott, J., Barnstable, C., and Hoh, J. (2005) Complement factor H polymorphism in age-related macular degeneration. *Science* 308, 385–389

3. Hageman, G. S., Anderson, D. H., Johnson, L. V., Hancox, L. S., Taiber, A. J., Hardisty, L. I., Hageman, J. L., Stockman, H. A., Borchardt, J. D., Gehrs, K. M., Smith, R. J., Silvestri, G., Russell, S. R., Klaver, C. C., Barbazetto, I., Chang, S., Yannuzzi, L. A., Barile, G. R., Merriam, J. C., Smith, R. T., Olsh, A. K., Bergeron, J., Zernant, J., Merriam, J. E., Gold, B., Dean, M., and Allikmets, R. (2005) A common haplotype in the complement regulatory gene factor H (HF1/CFH) predisposes individuals to age-related macular degeneration. *Proc. Natl. Acad. Sci. U.S.A.* 102, 7227–7232

4. Okamoto, H., Umeda, S., Obazawa, M., Minami, M., Noda, T., Mizota, A., Honda, M., Tanaka, M., Koyama, R., Takagi, I., Sakamoto, Y., Saito, Y., Miyake, Y., and Iwata, T. (2006) Complement factor H polymorphisms in Japanese population with age-related macular degeneration. *Mol. Vis.* 12, 156–158

5. Kondo, N., Honda, S., Ishibashi, K., Tsukahara, Y., and Negi, A. (2007) LOC387715/HTRA1 variants in polypoidal choroidal vasculopathy and age-related macular degeneration in a Japanese population. *Am. J. Ophthalmol.* 144, 608–612

6. Goto, A., Akahori, M., Okamoto, H., Minami, M., Terauchi, N., Haruhata, Y., Obazawa, M., Noda, T., Honda, M., Mizota, A., Tanaka, M., Hayashi, T., Tanito, M., Ogata, N., and Iwata, T. (2009) Genetic analysis of typical wet-type age-related macular degeneration and polypoidal choroidal vasculopathy in Japanese population. *J. Ocul. Biol. Dis. Infor.* 2, 164–175

7. Fritsche, L. G., Loenhardt, T., Janssen, A., Fisher, S. A., Rivera, A., Keilhauer, C. N., and Weber, B. H. (2008) Age-related macular degeneration is associated with an unstable ARMS2 (LOC387715) mRNA. *Nat. Genet.* 40, 892–896

8. Yang, Z., Tong, Z., Chen, Y., Zeng, J., Lu, F., Sun, X., Zhao, C., Wang, K., Davey, L., Chen, H., London, N., Muramatsu, D., Salasar, F., Carmona, R., Kasuga, D., Wang, X., Bedell, M., Dixie, M., Zhao, P., Yang, R., Gibbs, D., Liu, X., Li, Y., Li, C., Li, Y., Campochiaro, B., Constantine, R., Zack, D. J.,

9. Kanda, A., Chen, W., Othman, M., Branham, K. E., Brooks, M., Khanna, R., He, S., Lyons, R., Abecasis, G. R., and Swaroop, A. (2007) A variant of mitochondrial protein LOC387715/ARMS2, not HTRA1, is strongly associated with age-related macular degeneration. *Proc. Natl. Acad. Sci. U.S.A.* 104, 16227–16232

10. Kortvely, E., Hauck, S. M., Duetsch, G., Gloeckner, C. J., Kremmer, E., Alge-Priglinger, C. S., Deeg, C. A., and Ueffing, M. (2010) ARMS2 is a constituent of the extracellular matrix providing a link between familial and sporadic age-related macular degenerations. *Invest. Ophthalmol. Vis. Sci.* 51, 79–88

11. Shiga, A., Nozaki, H., Yokoseki, A., Nihonmatsu, M., Kawata, H., Kato, T., Koyama, A., Arima, K., Ikeda, M., Katada, S., Toyoshima, Y., Takahashi, H., Tanaka, A., Nakano, I., Ikeuchi, T., Nishizawa, M., and Onodera, O. (2011) Cerebral small-vessel disease protein HTRA1 controls the amount of TGF-β1 via cleavage of proTGF-β1. *Hum. Mol. Genet.* 20, 1800–1810

12. Zhang, L., Lim, S. L., Du, H., Zhang, M., Kozak, I., Hannum, G., Wang, X., Ouyang, H., Hughes, G., Zhao, L., Zhu, X., Lee, C., Su, Z., Zhou, X., Shaw, R., Geum, D., Wei, X., Zhu, J., Ideker, T., Oka, C., Wang, N., Yang, Z., Shaw, P. X., and Zhang, K. (2012) High temperature requirement factor A1 (HTRA1) gene regulates angiogenesis through transforming growth factor-β family member growth differentiation factor 6. *J. Biol. Chem.* 287, 1520–1526

13. Jiang, J., Huang, L., Yu, W., Wu, X., Zhou, P., and Li, X. (2012) Overexpression of HTRA1 leads to down-regulation of fibronectin and functional changes in RF/6A cells and HUVECs. *PLoS One* 7, e46115

14. Ferrer-Vaquer, A., Maurey, P., Werzowa, J., Firnberg, N., Leibbrandt, A., and Neubüser, A. (2008) Expression and regulation of HTRA1 during chick and early mouse development. *Dev. Dyn.* 237, 1893–1900

15. Chien, J., Ota, T., Aletti, G., Shridhar, R., Boccellino, M., Quagliuolo, L., Baldi, A., and Shridhar, V. (2009) Serine protease HtrA1 associates with microtubules and inhibits cell migration. *Mol. Cell. Biol.* 29, 4177–4187

16. Jones, A., Kumar, S., Zhang, N., Tong, Z., Yang, J. H., Watt, C., Anderson, J., Amrita, Fillerup, H., McCloskey, M., Luo, L., Yang, Z., Ambati, B., Marc, R., Oka, C., Zhang, K., and Fu, Y. (2011) Increased expression of multifunctional serine protease, HTRA1, in retinal pigment epithelium induces polypoidal choroidal vasculopathy in mice. *Proc. Natl. Acad. Sci. U.S.A.* 108, 14578–14583

17. Vierkotten, S., Muether, P. S., and Fauser, S. (2011) Overexpression of HTRA1 leads to ultrastructural changes in the elastic layer of Bruch's membrane via cleavage of extracellular matrix components. *PLoS One* 6, e22959

18. Hara, K., Shiga, A., Fukutake, T., Nozaki, H., Miyashita, A., Yokoseki, A., Kawata, H., Koyama, A., Arima, K., Takahashi, T., Ikeda, M., Shiota, H., Tamura, M., Shimoe, Y., Hirayama, M., Arisato, T., Yanagawa, S., Tanaka, A., Nakano, I., Ikeda, S., Yoshida, Y., Yamamoto, T., Ikeuchi, T., Kuwano, R., Nishizawa, M., Tsuji, S., and Onodera, O. (2009) Association of HTRA1 mutations and familial ischemic cerebral small-vessel disease. *N. Engl. J. Med.* 360, 1729–1739

19. Dewan, A., Liu, M., Hartman, S., Zhang, S. S., Liu, D. T., Zhao, C., Tam, P. O., Chan, W. M., Lam, D. S., Snyder, M., Barnstable, C., Pang, C. P., and Hoh, J. (2006) HTRA1 promoter polymorphism in wet age-related macular degeneration. *Science* 314, 989–992

20. Seddon, J. M., Ajani, U. A., and Mitchell, B. D. (1997) Familial aggregation of age-related maculopathy. *Am. J. Ophthalmol.* 123, 199–206

21. Seki, T., Yuasa, S., Oda, M., Egashira, T., Yae, K., Kusumoto, D., Nakata, H., Tohyama, S., Hashimoto, H., Kodaira, M., Okada, Y., Seimiya, H., Fusaki, N., Hasegawa, M., and Fukuda, K. (2010) Generation of induced pluripotent stem cells from human terminally differentiated circulating T cells. *Cell Stem Cell* 7, 11–14

22. Minegishi, Y., Iejima, D., Kobayashi, H., Chi, Z. L., Kawase, K., Yamamoto, T., Seki, T., Yuasa, S., Fukuda, K., and Iwata, T. (2013) Enhanced optineurin E50K-TBK1 interaction evokes protein insolubility and initiates familial primary open-angle glaucoma. *Hum. Mol. Genet.* 22, 3559–3567

23. Nakayama, M., Iejima, D., Akahori, M., Kamei, J., Goto, A., and Iwata, T. (2014) Overexpression of HtrA1 and exposure to mainstream cigarette

39

smoke leads to choroidal neovascularization and subretinal deposits in aged mice. *Invest. Ophthalmol. Vis. Sci.* **55,** 6514–6523

24. Yang, Z., Camp, N. J., Sun, H., Tong, Z., Gibbs, D., Cameron, D. J., Chen, H., Zhao, Y., Pearson, E., Li, X., Chien, J., Dewan, A., Harmon, J., Bernstein, P. S., Shridhar, V., Zabriskie, N. A., Hoh, J., Howes, K., and Zhang, K. (2006) A variant of the HTRA1 gene increases susceptibility to age-related macular degeneration. *Science* **314,** 992–993

25. Supanji, Shimomachi, M., Hasan, M. Z., Kawaichi, M., and Oka, C. (2013) HtrA1 is induced by oxidative stress and enhances cell senescence through p38 MAPK pathway. *Exp. Eye Res.* **112,** 79–92

26. Hansen, G., and Hilgenfeld, R. (2013) Architecture and regulation of HtrA-family proteins involved in protein quality control and stress response. *Cell Mol. Life Sci.* **70,** 761–775

27. Gray, C. W., Ward, R. V., Karran, E., Turconi, S., Rowles, A., Viglienghi, D., Southan, C., Barton, A., Fantom, K. G., West, A., Savopoulos, J., Hassan, N. J., Clinkenbeard, H., Hanning, C., Amegadzie, B., Davis, J. B., Dingwall, C., Livi, G. P., and Creasy, C. L. (2000) Characterization of human HtrA2, a novel serine protease involved in the mammalian cellular stress response. *Eur. J. Biochem.* **267,** 5699–5710

28. Foucaud-Scheunemann, C., and Poquet, I. (2003) HtrA is a key factor in the response to specific stress conditions in *Lactococcus lactis. FEMS Microbiol. Lett.* **224,** 53–59

29. Kleinman, M. E., Kaneko, H., Cho, W. G., Dridi, S., Fowler, B. J., Blandford, A. D., Albuquerque, R. J., Hirano, Y., Terasaki, H., Kondo, M., Fujita, T., Ambati, B. K., Tarallo, V., Gelfand, B. D., Bogdanovich, S., Baffi, J. Z., and Ambati, J. (2012) Short-interfering RNAs induce retinal degeneration via TLR3 and IRF3. *Mol. Ther.* **20,** 101–108

30. Tu, Z., Portillo, J. A., Howell, S., Bu, H., Subauste, C. S., Al-Ubaidi, M. R., Pearlman, E., and Lin, F. (2011) Photoreceptor cells constitutively express functional TLR4. *J. Neuroimmunol.* **230,** 183–187

31. Oka, C., Tsujimoto, R., Kajikawa, M., Koshiba-Takeuchi, K., Ina, J., Yano, M., Tsuchiya, A., Ueta, Y., Soma, A., Kanda, H., Matsumoto, M., and Kawaichi, M. (2004) HtrA1 serine protease inhibits signaling mediated by Tgfβ family proteins. *Development* **131,** 1041–1053

32. Wu, X., Chim, S. M., Kuek, V., Lim, B. S., Chow, S. T., Zhao, J., Yang, S., Rosen, V., Tickner, J., and Xu, J. (2014) HtrA1 is upregulated during RANKL-induced osteoclastogenesis, and negatively regulates osteoblast differentiation and BMP2-induced Smad1/5/8, ERK and p38 phosphorylation. *FEBS Lett.* **588,** 143–150

33. Zhu, F., Jin, L., Luo, T. P., Luo, G. H., Tan, Y., and Qin, X. H. (2010) Serine protease HtrA1 expression in human hepatocellular carcinoma. *Hepatobiliary Pancreat. Dis. Int.* **9,** 508–512

34. Xu, Y., Jiang, Z., Zhang, Z., Sun, N., Zhang, M., Xie, J., Li, T., Hou, Y., and Wu, D. (2013) HtrA1 downregulation induces cisplatin resistance in lung adenocarcinoma by promoting cancer stem cell-like properties. *J. Cell. Biochem.* **115,** 1112–1121

35. Ash, S. C., Yang, D. Q., and Britt, D. E. (2008) LYRIC/AEG-1 overexpression modulates BCCIPα protein levels in prostate tumor cells. *Biochem. Biophys. Res. Commun.* **371,** 333–338

36. Robertson, C. L., Srivastava, J., Siddiq, A., Gredler, R., Emdad, L., Rajasekaran, D., Akiel, M., Shen, X. N., Guo, C., Giashuddin, S., Wang, X. Y., Ghosh, S., Subler, M. A., Windle, J. J., Fisher, P. B., and Sarkar, D. (2014) Genetic deletion of AEG-1 prevents hepatocarcinogenesis. *Cancer Res.* **74,** 6184–6193

37. Huang, Y., and Li, L. P. (2014) Progress of cancer research on astrocyte elevated gene-1/metadherin (review). *Oncol. Lett.* **8,** 493–501

38. Noch, E., Bookland, M., and Khalili, K. (2011) Astrocyte-elevated gene-1 (AEG-1) induction by hypoxia and glucose deprivation in glioblastoma. *Cancer Biol. Ther.* **11,** 32–39

39. Domigan, C. K., and Iruela-Arispe, M. L. (2014) Stealing VEGF from thy neighbor. *Cell* **159,** 473–474

40. Li, K. Y., Tiruveedhula, P., and Roorda, A. (2010) Intersubject variability of foveal cone photoreceptor density in relation to eye length. *Invest. Ophthalmol. Vis. Sci.* **51,** 6858–6867

40

American Heart Association • American Stroke Association.

Endothelin-1 Induces Myofibrillar Disarray and Contractile Vector Variability in Hypertrophic Cardiomyopathy–Induced Pluripotent Stem Cell–Derived Cardiomyocytes

Atsushi Tanaka, MD; Shinsuke Yuasa, MD, PhD; Giulia Mearini, PhD; Toru Egashira, MD, PhD; Tomohisa Seki, MD, PhD; Masaki Kodaira, MD; Dai Kusumoto, MD; Yusuke Kuroda, MD; Shinichiro Okata, PhD; Tomoyuki Suzuki, MD, PhD; Taku Inohara, MD; Takuro Arimura, PhD; Shinji Makino, MD, PhD; Kensuke Kimura, MD, PhD; Akinori Kimura, MD, PhD; Tetsushi Furukawa, MD, PhD; Lucie Carrier, PhD; Koichi Node, MD, PhD; Keiichi Fukuda, MD, PhD

Background—Despite the accumulating genetic and molecular investigations into hypertrophic cardiomyopathy (HCM), it remains unclear how this condition develops and worsens pathologically and clinically in terms of the genetic–environmental interactions. Establishing a human disease model for HCM would help to elucidate these disease mechanisms; however, cardiomyocytes from patients are not easily obtained for basic research. Patient-specific induced pluripotent stem cells (iPSCs) potentially hold much promise for deciphering the pathogenesis of HCM. The purpose of this study is to elucidate the interactions between genetic backgrounds and environmental factors involved in the disease progression of HCM.

Methods and Results—We generated iPSCs from 3 patients with HCM and 3 healthy control subjects, and cardiomyocytes were differentiated. The HCM pathological phenotypes were characterized based on morphological properties and high-speed video imaging. The differences between control and HCM iPSC-derived cardiomyocytes were mild under baseline conditions in pathological features. To identify candidate disease-promoting environmental factors, the cardiomyocytes were stimulated by several cardiomyocyte hypertrophy-promoting factors. Interestingly, endothelin-1 strongly induced pathological phenotypes such as cardiomyocyte hypertrophy and intracellular myofibrillar disarray in the HCM iPSC-derived cardiomyocytes. We then reproduced these phenotypes in neonatal cardiomyocytes from the heterozygous *Mybpc3*-targeted knock in mice. High-speed video imaging with motion vector prediction depicted physiological contractile dynamics in the iPSC-derived cardiomyocytes, which revealed that self-beating HCM iPSC-derived single cardiomyocytes stimulated by endothelin-1 showed variable contractile directions.

Conclusions—Interactions between the patient's genetic backgrounds and the environmental factor endothelin-1 promote the HCM pathological phenotype and contractile variability in the HCM iPSC-derived cardiomyocytes. (*J Am Heart Assoc.* 2014;3: e001263 doi: 10.1161/JAHA.114.001263)

Key Words: disease modeling • ET-1 • HCM • iPS cells • *MYBPC3*

H ypertrophic cardiomyopathy (HCM) is characterized by unexplained hypertrophy in the left ventricle, diastolic dysfunction, increased interstitial fibrosis, and myofibrillar disarray.[1] HCM may lead to heart failure and sudden cardiac death.[2] The discovery of genetic mutations in patients with HCM led to an increased understanding of the underlying pathophysiology.[3] Because most of the genes associated with HCM encode components of the contractile apparatus of heart muscle, HCM was also termed a "disease of the sarcomere." Subsequent investigations confirmed that

mutations in genes encoding sarcomeric proteins cause HCM in humans and in genetically engineered mice.[4] However, it remains unclear how HCM develops clinically among patients with a wide variety of genetic backgrounds and how environmental factors could affect disease phenotypes.[5] A human disease model for HCM would be worthwhile to elucidate precise disease mechanisms. Moreover, better understandings of the mechanisms in HCM are needed to develop the required novel therapeutic strategies. Reprogramming of human somatic cells into induced pluripotent stem cells (iPSCs) potentially enables us to generate disease-specific iPSCs for in vitro genetic disease models and pharmacological screening.[6,7] In the past few years, many studies focusing on various types of human diseases, including cardiovascular arena, have yielded disease modeling by using patient-specific iPSCs.[8] The current study focused on elucidating a common pathway for progression of the HCM phenotype among patients with various genetic backgrounds by using HCM iPSC-derived cardiomyocytes.

More than 1000 distinct mutations in sarcomeric genes have been associated with HCM,[9] and the most frequent pathogenic mutations are found in *MYH7* and in *MYBPC3*, encoding β-myosin heavy chain and myosin binding protein C (cMyBP-C), respectively.[10] Mutations in sarcomeric proteins have been shown to increase myofilament calcium sensitivity and/or increase the energy requirements of myosin ATPase for efficient contractile dynamics in cardiomyocytes. Alterations in myocardial energetics and calcium handling combined with stimulation of signaling pathways might also diminish myocyte relaxation and promote myocyte growth, with resultant aberrations in tissue architecture.[5] However, it remains unknown when and how HCM phenotypes develop in patients. Patients with mutations may show no or only subtle phenotypes at a young age but develop severe hypertrophied heart as an adult, suggesting that environmental factors could influence the timing and extent of the disease phenotype. Understanding such mechanistic interactions between patient's genetic backgrounds and environmental factors is clearly necessary to develop novel therapies for HCM.[11]

Pathogenic mutations remain elusive in 30% to 40% of even stringently investigated HCM patients, making it difficult to generate effective and inclusive disease models.[3] However, patient-specific iPSCs could potentially be used to model HCM even in the absence of known mutations, because such cells contain the necessary patient's genomic information. In this study, we chose 3 unrelated patients with HCM—1 patient with a mutation in *MYBPC3*, to identify a common pathway for disease manifestation. We demonstrated that HCM iPSC-derived cardiomyocytes showed mild morphological phenotypes compared with the control under baseline conditions, but endothelin-1 (ET-1) induced pathological phenotypes such as cardiomyocyte hypertrophy and intracellular myofibrillar

disorganization, namely myofibrillar disarray, in the HCM iPSC-derived cardiomyocytes. Moreover, analysis of contractile dynamics in the isolated self-beating iPSC-derived cardiomyocytes by using high-speed video imaging with motion vector prediction[12] revealed variability in the direction of contraction among individual cardiomyocytes stimulated by ET-1. Finally, endothelin receptor type A blocker (ETA-b) clearly prevented the pathological features of HCM developing in the iPSC-derived cardiomyocytes. Our results indicate that specific interactions between the patient's genetic backgrounds and the environmental factor, ET-1, promoted the HCM phenotype in the iPSC-derived cardiomyocytes.

Methods

Human iPSC Generation

We generated iPSCs from 3 unrelated HCM patients and 3 healthy volunteers, respectively. In HCM patient 1 and controls 1 and 2, iPSCs were generated from skin dermal fibroblasts.[13] Six days after retrovirus transduction, fibroblasts were incubated with 0.05% trypsin/0.53 mmol/L EDTA (Gibco) and replated at 5×10^4 cells per 10-cm dish with mouse embryonic fibroblats (MEFs). Next day, the medium was replaced with human iPSC medium supplemented with 4 ng/mL bFGF. The medium was changed every day. Around 30 days after transduction, iPSC colonies were picked up. In addition, iPSCs of the other patients (HCM patients 2 and 3) and control 3 were established from T lymphocytes with Sendai virus encoding the same 4 factors.[14,15] Briefly, activated peripheral blood mononuclear cells were collected and transferred at 1.5×10^6 cells per well to a fresh anti-CD3 antibody–coated 6-well plate and incubated for an additional 24 hours. Then, the solution that contained Sendai virus vectors individually carrying each of *OCT3/4*, *SOX2*, *KLF4*, and *c-MYC* were added at a multiplicity of infection of 10. After 24 hours of infection, the medium was changed to fresh GT-T502 medium (KOHJIN BIO), and the cells were collected and split at 5×10^4 cells into 10-cm plates preseeded with MEFs. After an additional 24 hours, the medium was changed to human iPSC medium. Approximately 20 to 30 days after infection, iPSC colonies appeared and were picked up. These T-cell–derived iPSCs were maintained by using the same techniques as for those derived from dermal fibroblasts. Isolation and use of patient and control fibroblasts were approved by the Ethical Committee of Keio University (20-92-5) and performed after written consent was obtained.

Cell Culture

Dermal fibroblasts from a healthy volunteer and a patient with HCM (case 1) obtained through a dermal biopsy were

maintained in DMEM (Sigma) with 10% FBS (NICHIREI Biosciences Inc) and passaged twice. From a patient with HCM (case 2), peripheral blood mononuclear cells were separated via centrifugation of a heparinized whole blood sample, by using a Ficoll-Paque PREMIUM (GE Healthcare) gradient. The mononuclear cells were seeded onto the anti-human CD3 antibody (BD Pharmingen)-coated 6-well plates in 2 mL GT-T502 medium (KOHJIN BIO) per well and incubated for 5 to 7 days until the activated T cells reached 80% to 90% confluency. Human iPSCs were maintained on irradiated MEF feeder cells in human iPSC culture medium: 80% DMEM/F12 (Sigma), 20% KO Serum Replacement (Invitrogen), 4 ng/mL basic fibroblast growth factor (bFGF; WAKO), 2 mmol/L L-glutamine (Invitrogen), 0.1 mmol/L nonessential amino acids (Sigma), 0.1 mmol/L 2-mercaptoethanol, 50 U/mL penicillin, and 50 mg/mL streptomycin (Invitrogen). The medium was changed every 2 days, and the cells were passaged by using 1 mg/mL collagenase IV (Invitrogen) every 5 to 7 days.

Virus Preparation (Lentivirus, Retrovirus, and Sendai Virus)

Lentiviruses were generated by cotransfecting the pLenti6/UbC encoding the mouse *Slc7a1* together with the Virapower packaging mix (pLP1, pLP2, and pLP/VSVG mixture) by Lipofectamine 2000 (Invitrogen), according to the manufacturer's instructions, into 293FT cells seeded at 4×10^6 cells per 10-cm dish. Lentiviruses were collected 36 hours after transfection and filtrated through a 0.45-μm-pore cellulose acetate filter. The virus-containing supernatant supplemented with 4 μg/mL polybrene (Wako) was added to the human fibroblasts seeded at 8×10^5 cells per 10-cm dishes and incubated for 24 hours at 37°C, 5% CO_2. The pMXs retroviral vectors contained the 5′-long terminal repeat (LTR) and 3′-LTR of Moloney murine leukemia virus, encoded human *OCT3/4*, *SOX2*, *KLF4*, and *c-MYC* genes, and the green fluorescence protein to monitor transfection efficacy. PLAT-E packaging cells, which were derived from 293T cells and contain env-IRES-puro and gag-pol-IRES-bs cassettes driven by the EF1-α promoter (Cell biolabs, Inc.), were plated at 3.6×10^6 cells per 10-cm dish and incubated overnight. Next day, the cells were transfected with pMXs vectors with Fugene 6 transfection reagent (Roche). Forty-eight hours after transfection, the medium was collected, and the virus-containing supernatants were filtered through a 0.45-μm-pore filter and supplemented with 4 μg/mL polybrene (Wako). Equal parts of supernatants containing the 4 retroviruses were mixed, transferred to the fibroblasts expressing mouse *Slc7a1* gene seeded at 8×10^5 cells per 10-cm dish, and incubated overnight. Sendai virus vectors, carrying the same 4 specific transcriptional factors independently, were commercially obtained (CytoTune-iPS Reprogramming Kit; Invitrogen).

Teratoma Formation

To confirm pluripotency in vivo, teratoma formation was assessed in accordance with the Institutional Animal Care and Use Committee of Keio University. Approximately 1 to 2×10^6 iPSCs were injected into the testis of anesthetized immuno-compromised NOD-SCID mice (CREA-Japan). Ten to 12 weeks after injection, the mice were euthanized, and teratomas were excised, fixed overnight in formalin, embedded in paraffin, and analyzed by using hematoxylin–eosin staining. The mice were anesthetized by using a mixture of ketamine (50 mg/kg), xylazine (10 mg/kg), and chlorpromazine (1.25 mg/kg). The adequacy of anaesthesia was monitored by heart rate, muscle relaxation, and loss of sensory reflex response (ie, nonresponse to tail pinching). The investigation conforms with the "Guide for the Care and Use of Laboratory Animals" published by the US National Institutes of Health (NIH Publication No. 85-23, revised 1996).

Genetic Analyses

DNA samples extracted from the peripheral blood of subjects were used as templates to amplify each coding exon of *MYBPC3*, *MYL2*, *MYL3*, *TNNT2*, *TNNI3*, *TPM1,* and *ACTC* and exons 3 to 25 of *MYH7* by using polymerase chain reaction (PCR). Sequences of primers and the PCR conditions used in this study are available on request. PCR products were analyzed for sequence variations through direct DNA sequencing of both strands by using Big Dye Terminator chemistry (version 3.1) and ABI3100 DNA Analyzer (Applied Biosystems). The sequence variations found in the patients were considered to be mutations on the basis of following criteria: (1) presence in all tested affected members of the family of each proband patient, (2) absence from 400 unrelated chromosomes of the control subjects, (3) absence from a public database of polymorphism, dbSNP database (http://www.ncbinlm.nih.gov/projects/SNP/), (4) mutations at the evolutionary conserved residues, and/or (5) identification as an HCM-causing mutation in previous reports. All subjects received informed consent for blood testing for genetic abnormalities associated with hereditary HCM.

In Vitro Cardiomyocyte Differentiation and Isolation

For embryoid body (EB)-formed differentiation, iPSCs colonized on MEFs were detached by using 1 mg/mL type IV collagenase (Invitrogen) and suspended on ultra-low attachment plates (Corning) with differentiation medium, consisting of 80% Minimum Essential Medium Alpha Medium (Gibco), 2 mmol/L L-glutamine (Invitrogen), 0.1 mmol/L nonessential amino acids (Sigma), 0.1 mmol/L 2-mercaptoethanol, 50 U/mL penicillin–50 mg/mL streptomycin (Invitrogen), and 20%

FBS (Gibco) to initiate cardiac differentiation. During suspension culture, the medium was changed every 2 days in the first week and then every week with the differentiation medium with 5% FBS. After 20 to 30 days of differentiation, self-contracting EBs were picked up and replaced in the other ultra-low attachment plates (Corning). For immunohistochemical and physiological motion analyses, the singled cardiomyocytes isolated from spontaneously contracting EBs by using 0.25% trypsin (Invitrogen), 1 mg/mL type IV collagenase (Invitrogen), and ADS buffer (NaCl 116 mmol/L, KCl 5.4 mmol/L, NaH_2PO_4 1mmol/L, $MgSO_4$ 0.8 mmol/L, Glucose 5.5 mmol/L, HEPES 20 mmol/L, pH 7.35 adjusted by NaOH) for 30 minutes at 37°C were plated onto fibronectin-coated dishes and incubated for 1 week with or without the pharmacological agents (eg, ET-1) in the presence of 20% FBS. To analyze the iPSC-derived cardiomyocyte, the mixtures of contracting EBs derived from 1 to 3 independent iPSC lines were used in each case.

Isolation of Neonatal Mouse Cardiomyocytes

Neonatal mouse cardiomyocytes were isolated and cultured following a well-established protocol,[16] according to the "Guide for the Care and Use of Laboratory Animals." After 3 days of culture, serum was reduced to 0.2% for 12 hours before stimulation with 100 nmol/L ET-1 for an additional 48 hours. Cells were then harvested for RNA analysis or fixed for immunofluorescence staining.

Immunofluorescence Microscopy

Undifferentiated iPSCs plated on coverslips with MEFs or differentiated cardiomyocytes plated onto fibronectin-coated dishes were washed once with D-PBS(−) (Wako) and fixed with 4% Paraformaldehyde Fixative (MUTO Pure Chemicals) at 4°C for 30 minutes. After fixation, cells were treated with 0.4% Triton X-100 (when targeted intracellular labeling) in PBS for 15 minutes at room temperature. After being blocked with ImmunoBlock (DS Pharma Biomedical) for 5 minutes 3 times, cells were incubated at 4°C overnight with the primary antibody, followed by washing with the blocking medium and incubation at room temperature for 60 minutes with the corresponding secondary antibody. Nuclei were stained with 50 ng/mL DAPI (Invitrogen) for 5 minutes at room temperature. Fluorescent signals were detected by the use of fluorescence laser microscope (BZ-9000, Keyence) equipped with a 1.5×10^5 pixel charged coupled device camera. Neonatal mouse cardiomyocytes were plated onto laminin-coated coverslips and washed twice with PBS before fixation in methanol: acetone (20:80) for 10 minutes at −20°C. Cells were permeabilized 1 hour at room temperature with 0.5% Triton X-100, 1% BSA, and 10% FCS in PBS. After washing with 0.5% Triton X-100 and 1% BSA in PBS, neonatal mouse cardiomyo-

cytes were incubated for 3 hours at room temperature with primary antibodies diluted in the same solution. Cells were then rinsed twice (0.5% Triton X-100, 1% BSA in PBS) and incubated for 1 hour at room temperature in the dark with secondary antibodies diluted in the same dilution. At the same time, nuclei were stained with 5 μmol/L DRAQ5 (Biostatus). After 3 washes in PBS, cells were mounted with Mowiol, and fluorescence was analyzed by confocal microscopy by using a Zeiss Axiovert microscope with a ×40 oil objective.

Electron Microscopy

Contracting EBs were fixed with 2.5% glutaraldehyde in 60 mmol/L HEPES, pH 7.4, for 2 hours at room temperature and washed 3 times with 0.2 mol/L phosphate buffer. Secondary fixation were performed with 1% OsO_4 in 60 mmol/L HEPES, pH 7.4, for 120 minutes at room temperature. For en bloc stain, 2% uranyl acetate was used for 30 minutes at room temperature. Tissues were dehydrated with gradually increasing concentration of ethanol and embedded by plain resin, before sectioning and staining.

Quantitative Reverse Transcription–PCR

For quantitative reverse transcription (RT)–polymerase chain reaction (PCR) assays, total RNA was extracted from 30 days beating EBs by using TriZOL Reagent (Invitrogen) and TURBO DNA-*free* kit (Ambion), according to the manufacturers' instructions. One microgram of total RNA was reverse transcribed into cDNA by using the SuperScript II Reverse Transcriptase (Invitrogen). Quantitative RT-PCR for endothelin receptor type A (*EDNRA*) and B (*EDNRB*) was performed by using TaqMan Gene Expression Assays (*EDNRA*; Hs03988672_m1, *EDNRB*; Hs00240747_m1) and TaqMan Universal PCR Master Mix (Applied Biosystems). Quantitative RT-PCR for *TNNT2* was performed by using Perfect Real Time SYBR *Premix Ex Taq* II kit (Takara) with the primer set TTCACCAAAGATCTGCTCCTCGCT and TTATTACTGGTGTGGA GTGGGTGTGG. Samples were cycled 40 times by using a 7500 Real Time PCR System (Applied Biosystems), and cycle conditions were as follows: 2 minutes at 50°C, 10 minutes at 95°C, followed by 40 cycles of 15 seconds at 95°C and 60 seconds at 60°C. Cycle threshold was calculated under default settings by using real-time sequence detection software (Applied Biosystems). The expression levels of *EDNRA* and *EDNRB* were normalized to that of *TNNT2*.

Quantification of Gene Expression in Mice

For RT and quantitative PCR, ReverTraAce qPCR RTMaster Mix with gDNA Remover (TOYOBO) and THUNDERBIRD SYBR qPCR Mix (TOYOBO) were used according to manufacturers'

44

instructions. Primer sequences of the targeted genes are as follows: α-skeletal actin (*Acta1*) forward: CCCCTGAGGAG CACCCGACT, reverse: CGTTGTGGGTGACACCGTCCC; atrial natriuretic peptide (ANP) (*Nppa*) forward: TCGTCTTGGCCT TTTGGCT, reverse: TCCAGGTGGTCTAGCAGGTTCT; B-type natriuretic peptide (*Nppb*) forward: AAGTCCTAGCCAGTCTCCAGA, reverse: GAGCTGTCTCTGGGCCATTTC; guanine nucleotide binding protein, alpha stimulating (*Gnas*) F: CAAGGCTC TGTGGGAGGAT, reverse: CGAAGCAGGTCCTGGTCACT. Samples were cycled 40 times by using a 7500 Real Time PCR System (Applied Biosystems) and cycle conditions were as follows: 60 seconds at 95°C followed by 40 cycles of 15 seconds at 95°C and 35 seconds at 60°C. Cycle threshold was calculated under the default settings by real-time sequence detection software (Applied Biosystems). The expression levels of *Acta1*, *Nppa*, and *Nppb* were normalized to that of *Gnas*.

iPSC-Derived Cardiomyocyte Size Measurement

On 30, 60, or 90 days after differentiation, the single cardiomyocytes were isolated from contracting EBs and immunolabeled for anti-cardiac troponin T with Alexa Fluor 594 goat anti-mouse IgG$_1$ as described earlier, and the surface areas of the single cardiomyocytes derived from HCM patients' and healthy volunteers' iPSCs were measured by using computerized morphometric system (ImageJ software, NIH).

Western Blot Analysis

Proteins from self-beating EBs were extracted with RIPA buffer (Nacalai tesque). The proteins were loaded on the Mini-PROTEAN TGX Gels (Bio-Rad, 4% to 15%) and then electrically separated and transferred onto 0.45-μm-pore size nitrocellulose blotting membranes (GE Healthcare). The membranes were stained with antibodies directed against cMyBP-C (1:100; Santa Cruz), cardiac troponin T (cTnT) (1:200; Santa Cruz), α-actinin (1:2500; Sigma), ANP (1:200; Santa Cruz), or GAPDH (1:500; Cell Signaling) overnight at 4°C. After being washed in TBS buffer containing 0.1% Tween 20, the membranes were incubated with appropriate horseradish peroxidase–conjugated secondary antibodies (anti-mouse HRP 1:2000, anti-rabbit HRP 1:2000, or anti-goat HRP 1:2000, respectively) for 1 hour at room temperature. The immunoreactive bands were visualized by Chemi-Lumi One L (Nacalai tesque) and subsequently detected by the Image Reader LAS-3000 (FUJIFILM). Quantification of the signals was conducted by using the NIH ImageJ software.

Reagents

Immunofluorescence staining for pluripotency of iPSCs was performed by using the following primary antibodies:

anti-NANOG (Abcam), anti-OCT3/4 (Santa Cruz), anti-SSEA 3 (Millipore), anti–SSEA 4 (Millipore), anti–Tra-1-60 (Millipore), and anti–Tra-1-81 (Millipore). In immunofluorescence staining for cardiac markers, monoclonal anti–α-actinin (Sigma), monoclonal anti-cTnT (Thermo Scientific), polyclonal anti-cTnT (Santa Cruz), monoclonal anti–myosin light chain (MLC)2a (Synaptic Systems), polyclonal anti-MLC2v (ProteinTech Group), anti-ANP (Santa Cruz), anti–cMyBP-C (Santa Cruz), polyclonal anti–cMyBP-C motif (supplied by C. Witt University of Heidelberg, Heidelberg, Germany), and anti–nuclear factor of activated T cells (NFAT)c4 (Santa Cruz) were used. The isotype-specific secondary antibodies, Alexa Fluor 488 chicken anti-rabbit IgG, Alexa Fluor 594 goat anti-mouse IgG$_1$, Alexa Fluor 488 goat anti-rat IgM, Alexa Fluor 594 goat anti-mouse IgM, Alexa Fluor 488 goat anti-mouse IgG, Alexa Fluor 594 goat anti-mouse IgG$_{2b}$, Alexa Fluor 594 chicken anti-goat IgG, and Alexa Fluor 555 goat anti-rabbit IgG, were all obtained from Invitrogen. The tested drugs included endothelin-1 (1.0, 10, 100, or 1000 nmol/L), angiotensin II (100 nmol/L), insulin-like growth factor 1 (100 nmol/L), phenylephrine (0.05 mmol/ L), BQ-123 (250 nmol/L), and BQ-788 (100 nmol/L) (all from Sigma).

High-Speed Video Microscopy

Isolated cardiomyocytes were cultured in a well of 24-well plate and incubated with 500 μL of culture medium. A high-speed digital CMOS camera (KP-FM400WCL; Hitachi Kokusai Electric) was mounted on an inverted microscope (Eclipse TE2000; Nikon), which was equipped with a *xy* scanning stage (Bios-T; Sigma Koki). The microscope was also equipped with a stage-top mini-incubator (WSKM; Tokai Hit), which maintained the temperature of the culture plate at 37°C, 5% CO_2. Videos of cardiomyocytes maintained in DMEM were recorded as sequential phase-contrast images with a ×10 or ×20 objective at a frame rate of 150 fps, a resolution of 512×512 pixels, and a depth of 8 bits.

Evaluation of Contraction Direction With Motion Vector Prediction Algorithm

The contraction and relaxation motion of cardiomyocytes were evaluated from the high-speed video imaging by using the motion vector prediction method.[12] Briefly, each frame was divided into square blocks of $N \times N$ pixels. Then, for a maximum motion displacement of w pixels per frame, the current block of pixels was matched to the corresponding block at the same coordinates in the previous frame within a square window of width $N+2w$. (Optimal values of N and w for the cardiac motion detection may vary with the observation magnification and resolution of the camera. Here, we set

---

Table. Detailed Parameters of the Cell Surface Area and the Prevalence of Myofibrillar Disarray

	Control		HCM	
	Cell Area	Myofibrillar Disarray	Cell Area	Myofibrillar Disarray
Figures 5C and 6D				
Day 30	N=798 (sample size)	6.5% (prevalence) 55/851 (number of cardiomyocytes)	N=823	8.9% 84/947
	93 133 (mean)		109 933	
	81 510 (median)		97 480	
	61 200 to 109 930 (interquartile range)		69 245 to 132 820	
Day 60	N=811	5.6% 49/875	N=816	9.2% 92/995
	92 636		112 592	
	80 160		94 060	
	58 760 to 110 940		68 560 to 140 740	
Day 90	N=810	5.0% 47/932	N=821	9.3% 83/895
	91 319		113 097	
	79 760		96 880	
	61 140 to 107 120		67 230 to 13 0740	
Figure 9B through E				
Free (day 60)	N=811	5.6% 49/875	N=816	9.2% 92/995
	92 636		112 592	
	80 160		94 060	
	58 760 to 110 940		68 560 to 140 740	
ET-1	N=789	6.2% 59/955	N=809	20.6% 197/956
	102 499		135 038	
	89 080		116 280	
	68 200 to 119 120		85 120 to 165 690	
Ang II	N=811	5.8% 51/883	N=788	9.2% 80/865
	94 848		121 538	
	83 560		102 360	
	61 400 to 117 220		77 100 to 144 250	
IGF-1	N=817	6.4% 58/903	N=810	10.1% 85/844
	97 786		120 339	
	85 800		103 880	
	65 600 to 113 480		77 160 to 140 470	
PE	N=819	6.4% 56/870	N=819	10.3% 88/857
	99 371		120 147	
	88 080		101 657	
	66 900 to 118 200		70 160 to 143 130	
Figure 12A and 12B				
ET-1, 0 nmol/L (day 60)	N=811	5.6% 49/875	N=816	9.2% 92/995
	92 636		112 592	
	80 160		94 060	

ORIGINAL RESEARCH

Table. Continued

	Control		HCM	
	Cell Area	Myofibrillar Disarray	Cell Area	Myofibrillar Disarray
	58 760 to 110 940		68 560 to 140 740	
ET-1, 1.0 nmol/L	N=822	5.7% 51/889	N=818	13.8% 121/878
	94 228		122 839	
	81 460		105 798	
	61 920 to 112 045		72 355 to 154 155	
ET-1, 10 nmol/L	N=811	5.9% 52/878	N=822	16.7% 152/908
	98 535		127 885	
	86 680		106 940	
	64 920 to 118 350		77 380 to 152 398	
ET-1, 100 nmol/L	N=789	6.2% 59/955	N=809	20.6% 197/956
	102 499		135 038	
	89 080		116 280	
	68 200 to 119 120		85 120 to 165 690	
ET-1, 1000 nmol/L	N=810	6.4% 58/907	N=819	22.9% 204/892
	105 608		142 510	
	94 040		122 040	
	71 857 to 125 420		87 160 to 163 720	
Figure 13B and 13C (graphs of control not shown)				
Free (day 60)	N=811	5.6% 49/875	N=816	9.2% 92/995
	92 636		112 592	
	80 160		94 060	
	58 760 to 110 940		68 560 to 140 740	
ET-1	N=789	6.2% 59/955	N=809	20.6% 197/956
	102 499		135 038	
	89 080		116 280	
	68 200 to 119 120		85 120 to 165 690	
ET-1+ETA-b	N=806	5.1% 47/916	N=817	10.4% 94/902
	91 901		116 527	
	81 640		103 280	
	63 515 to 108 460		73 200 to 140 880	
ET-1+ETB-b	N=809	5.0% 43/866	N=821	17.3% 152/880
	98 786		132 030	
	88 360		116 000	
	66 880 to 116 400		81 010 to 159 690	
ET-1+ETA-b+ETB-b	N=808	5.5% 50/907	N=825	10.7% 98/917
	93 311		117 891	
	83 300		100 800	
	63 538 to 110 918		75 440 to 142 080	
ETA-b+ETB-b	N=814	5.6% 52/927	N=823	9.5% 87/913
	92 227		110 616	
	81 740		94 650	

Continued

47

Table. Continued

	Control		HCM	
	Cell Area	Myofibrillar Disarray	Cell Area	Myofibrillar Disarray
	62 760 to 108 855		65 360 to 138 800	
Figure 14C and 14D (experiments in control not performed)				
Free–free			N=300	13.9%
			137 988	44/317
			121 350	
			89 755 to 159 190	
Free–ET-1			N=300	26.7%
			172 995	92/344
			160 570	
			117 113 to 212 515	
ET-1–free			N=300	34.9%
			188 432	126/361
			158 215	
			121 758 to 220 150	
ET-1–ETA-b			N=300	20.8%
			142 950	69/332
			128 160	
			96 530 to 174 118	
Figure 15C and 15D	WT		HET	
Control	N=176	4.7%	N=173	8.1%
	40 517	10/215	44 712	18/223
	38 073		45 126	
	29 234 to 49 326		31 353 to 55 272	
ET-1	N=174	5.1%	N=178	15.5%
	52 694	12/236	57 824	36/233
	47 285		55 712	
	35 484 to 68 430		43 746 to 69 539	

HCM indicates hypertrophic cardiomyopathy; ET-1, endothelin-1; Ang II, angiotensin II; IGF-1, insulin-like growth factor-1; PE, phenylephrine; ETA-b, endothelin receptor type A blocker; ETB-b, endothelin receptor type B blocker; HET, heterozygous *Mybpc3*-targeted knock-in mice; WT, wild-type.

$N=16$ and $w=4$. These values were determined empirically based on the throughput speed of calculation and accuracy of the block-matching detection.) The best match on the basis of a matching criterion yielded the displacement. The mean absolute error was used as the matching criterion. The matching function is given by

$$M(i,j) = \frac{1}{N^2} \sum_{m=1}^{N} \sum_{n=1}^{N} |f_t(m,n) - f_{t-1}(m+i, n+j)|$$
$$-w \leq i, j \leq w$$

where $f_t(m, n)$ represents the intensity at coordinates (m, n) in the current block of $N \times N$ pixels and $f_{t-1}(m+i, n+j)$ represents the intensity at new coordinates $(m+i, n+j)$ in the corresponding block in the previous frame. We performed this calculation for every 4×4 pixels in the image and obtained the motion vectors of cardiomyocyte motion. Because the contraction and relaxation of cardiomyocytes occur nearly symmetrical direction, the vector angle histogram tends to show 2 peaks with 180° interval. By summing up the histogram at the center of the peaks, we averaged the histogram for calculation of standard deviation (SD) score, as illustrated later in Figure 16. Thus, vector angles (between each vector and x-axis [horizontal-axis]) were evaluated during the contraction and relaxation process and were summarized in the vector angle histograms (see Figure 17).
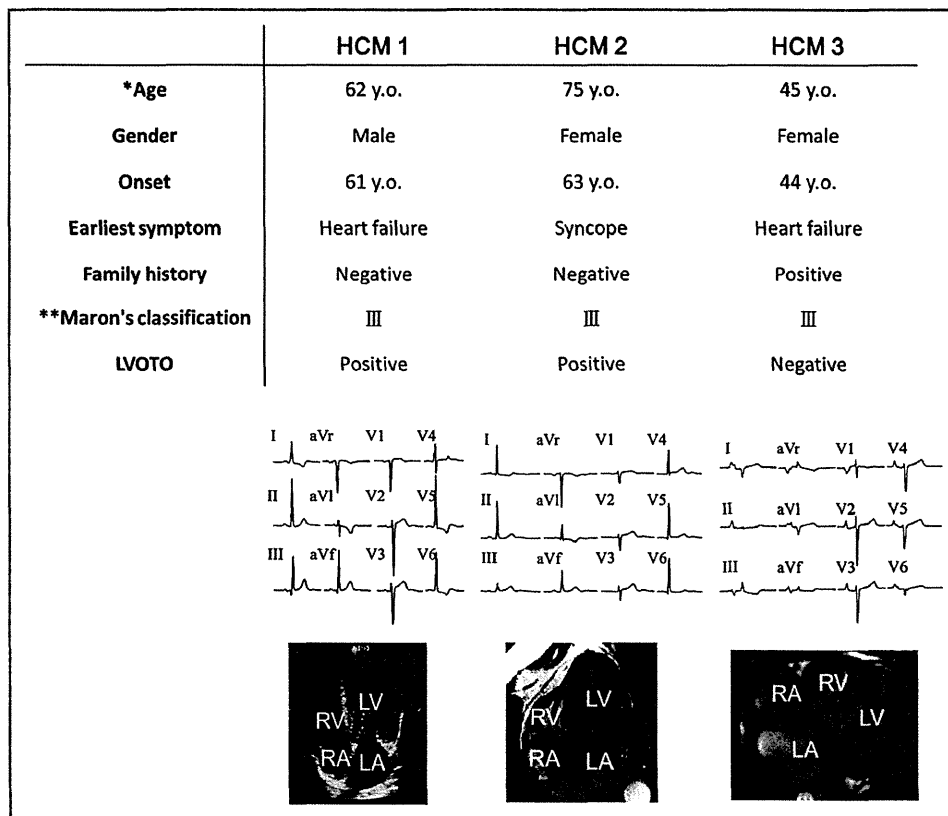
48

	HCM 1	HCM 2	HCM 3
*Age	62 y.o.	75 y.o.	45 y.o.
Gender	Male	Female	Female
Onset	61 y.o.	63 y.o.	44 y.o.
Earliest symptom	Heart failure	Syncope	Heart failure
Family history	Negative	Negative	Positive
**Maron's classification	III	III	III
LVOTO	Positive	Positive	Negative

Figure 1. Patients' clinical characteristics. Detailed clinical informations, electrocardiogram, and 4-chamber images of echocardiogram or cardiac magnetic resonance imaging of each patient with HCM. *The age when the one's iPSCs were established. **Maron's classification.[19] HCM indicates hypertrophic cardiomyopathy; iPSCs, induced pluripotent stem cells; LA, left atrium; LV, left ventricle; LVOTO, left ventricular outflow tract obstruction; RA, right atrium; RV, right ventricle.

Statistical Analysis

This study was designed to address the differences in the environmental factor–induced pathological responsiveness between control and HCM iPSC-derived cardiomyocytes and to determine the key environmental factors involved in the pathological mechanisms in HCM. Continuous data were presented as mean±SEM. The differences of the continuous data in 2 groups were evaluated by using the Mann–Whitney U test or Student t test. One-way ANOVA with Steel's multiple comparison post-test or Kruskal–Wallis test was used for >2 groups where appropriate. Categorical data were compared by using the χ^2 test. "Control" and "HCM" depicted in the graphs represent the total results including control 1, 2, and 3 or HCM 1, 2, and 3, respectively. Sample size and analysis methods used in each experiment are described in each figure legend. Detailed parameters of the cell surface area and the prevalence of myofibrillar disarray are listed in Table. All analyses were conducted by using JMP 10 (SAS Institute

Japan), and a value of $P<0.05$ was defined as statistically significant.

Results

Generation of HCM iPSC-Derived Cardiomyocytes

We selected 3 unrelated patients with HCM (Figure 1). Among them, 2 showed typical clinical manifestation without family history (HCM patients 1 and 2), without mutations in the sarcomeric genes related to HCM,[9] such as *MYH7*, *MYBPC3*, *TNNT2*, *TNNI3*, *MYL2*, *MYL3*, and *ACTC1*. We also chose a third patient who showed typical clinical manifestation of HCM with family history and with a mutation in *MYBPC3* (Gly999-Gln1004del; HCM 3). As controls, we recruited 1 independent healthy volunteer and used 2 other, previously characterized, control iPSC lines (controls 2 and 3).[17,18] In HCM patient 1 and controls 1 and 2, iPSCs were generated from skin dermal fibroblasts with retrovirus carrying each of

OCT3/4, SOX2, KLF4, and *c-MYC.*[6] iPSCs of the other patients (HCM 2 and 3) and control 3 were established from T lymphocytes of peripheral blood with Sendai virus carrying the same transcriptional factors.[14,17] Generated iPSCs showed appropriate stem cell marker expression (Figure 2A) as well as multipotency based on teratoma formation containing

tissues derived from all 3 germ layers (Figure 2B). Subsequently, cardiomyocytes were differentiated from the iPSCs by EB formation. Immunostaining revealed that the iPSC-derived cardiomyocytes expressed cardiomyocyte-specific markers α-actinin, MLC2a, MLC2v, cTnT, and ANP (Figure 3A through 3C).
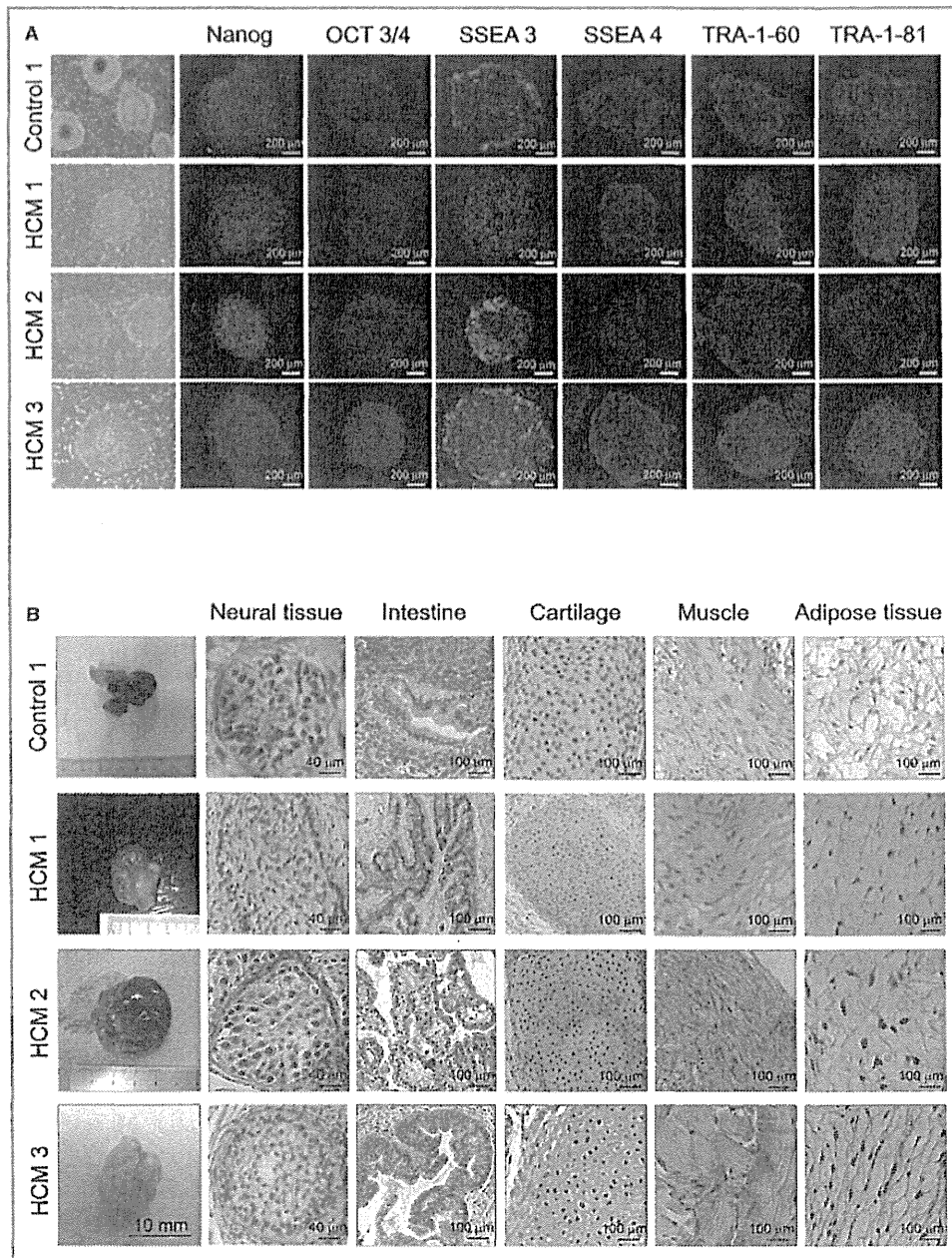
Figure 2. iPSC generation from control and patients with HCM. A, Immunostaining for human pluripotent stem cell markers, *Nanog, OCT 3/4, SSEA 3, SSEA 4, TRA-1-60,* and *TRA-1-81.* B, Teratoma formation from control 1 , HCM 1 , HCM 2, and HCM3 iPSCs in the immunocompromised NOD-SCID mice. Sections of teratomas were stained with hematoxylin–eosin, and tissues representative of all 3 germ layers were observed. HCM indicates hypertrophic cardiomyopathy; iPSCs, induced pluripotent stem cells.
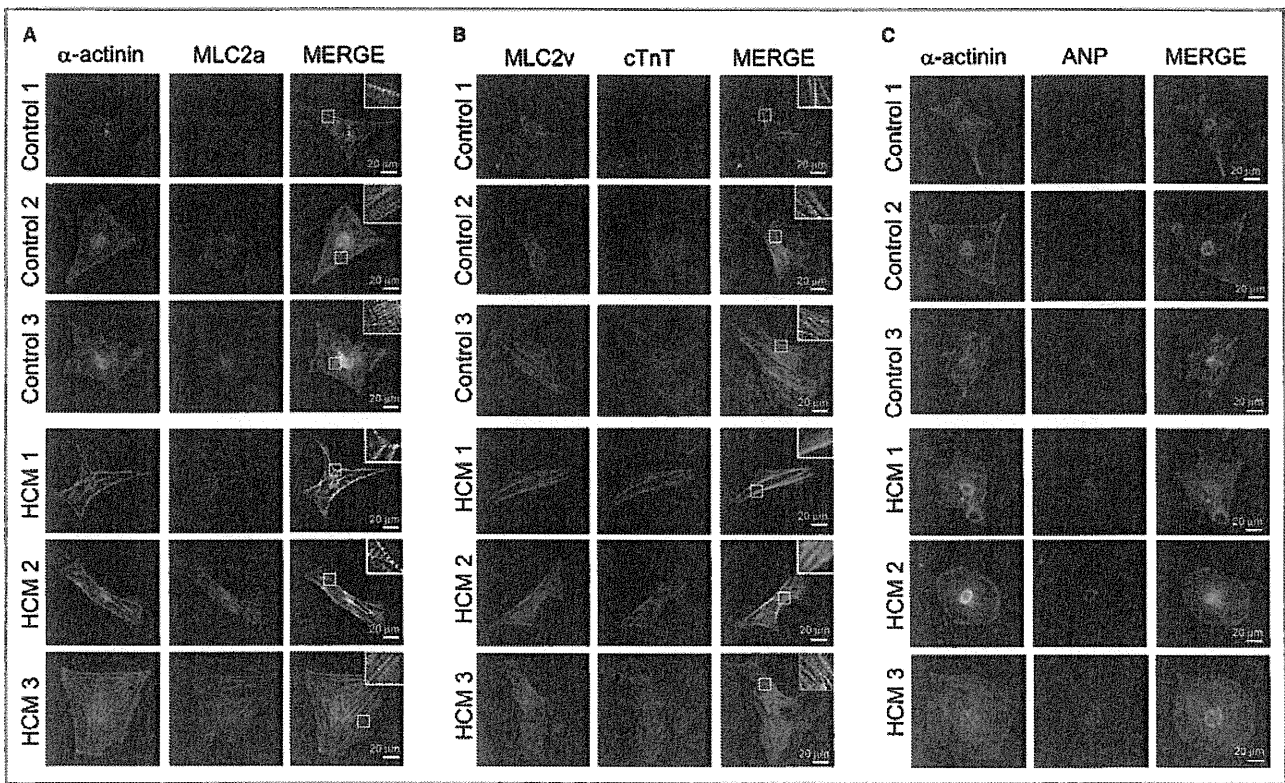
Figure 3. Cardiomyocyte generation from control and HCM iPSCs. The single cardiomyocytes at 60 days after differentiation were cultured for 7 days under adherent culture conditions. A, Immunostaining for α-actinin and MLC2a with DAPI nuclear staining in the single cardiomyocytes derived from each iPSC. B, Immunostaining for MLC2v and cTnT with DAPI nuclear staining in the single cardiomyocytes derived from each iPSCs. C, Immunostaining for α-actinin and ANP with DAPI nuclear staining in the single cardiomyocytes derived from each iPSC. ANP indicates atrial natriuretic peptide; cTnT, cardiac troponin T; DAPI, 4′,6-diamidino-2-phenylindole; HCM, hypertrophic cardiomyopathy; iPSCs, induced pluripotent stem cells; MLC2a, myosin light chain 2a; MLC2v, myosin light chain 2v.

Pathological Features of HCM iPSC-Derived Cardiomyocytes

Cardiomyocyte hypertrophy is a well-known pathological characteristic of HCM.[9] To reveal the size and shape of iPSC-derived cardiomyocytes, we dissociated them from EBs (30, 60, and 90 days after differentiation) and cultured them under adherent culture conditions for 7 days (Figure 4). We then measured cell surface area after immunostaining for cTnT and α-actinin (Figure 5A and 5B). Although there were no time-dependent changes in the cell surface area, the HCM iPSC-derived cardiomyocyte surface areas were mildly but significantly larger at each time point (Figure 5C). To further investigate the fine cellular organization, the beating EBs were examined at day 60 by using electron microscopy. Well-organized striated myofibrils were observed in beating EBs derived from control and HCM iPSCs (Figure 6A), but frequent myofibrillar disarrays were found in the HCM iPSC-derived cardiomyocytes (Figure 6B). In HCM hearts, cardiomyocytes often show this type of morphological disorganization, which is related to the cardiomyocyte pathophysiology in HCM,[20–22] and it is consequently
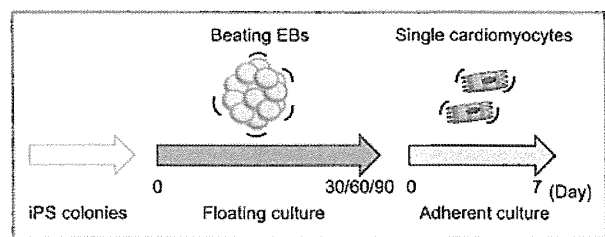

Figure 4. Time course of drug stimulation protocols for beating single cardiomyocytes. EBs were formed under floating culture conditions at day 0 and then maintained until 30, 60, or 90 days. The floating EBs were then enzymatically dissociated and single cardiomyocytes were cultured under adherent conditions for 7 days. EBs indicates embryoid bodies; iPS, induced pluripotent stem.

used as a marker of the disease in this study. Immunostaining of the iPSC-derived cardiomyocytes for cTnT also could highlight the myofibrillar disarray (Figure 6C). To quantitatively evaluate the frequency of this morphological characteristic, we defined the cardiomyocyte with myofibrillar disarray as >50% of
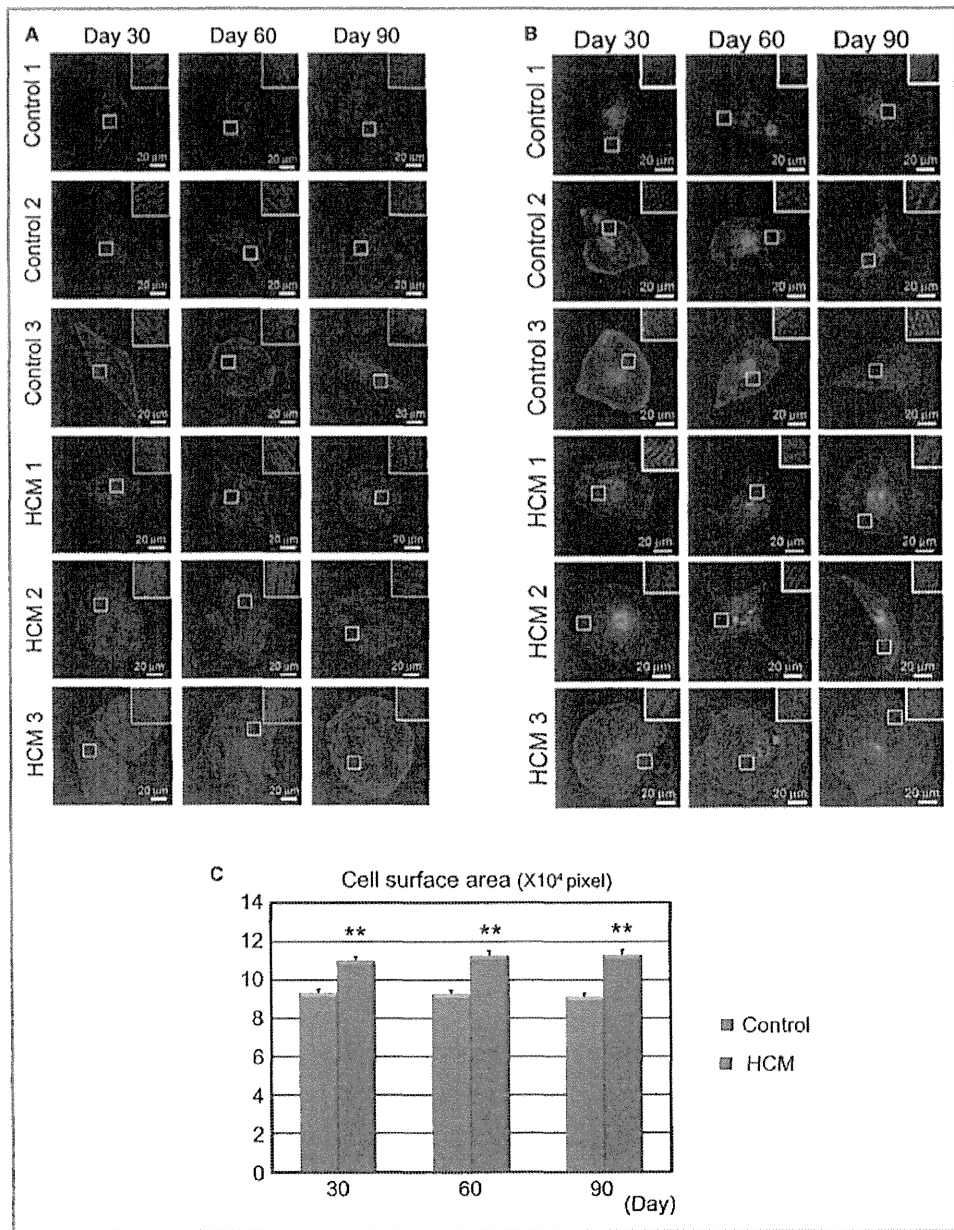
51

Figure 5. In vitro pathological findings: cell surface area in the isolated iPSC-derived cardiomyocytes. Embryoid bodies (EBs) were maintained for 30, 60, or 90 days in floating culture. After dissociation, cardiomyocytes were cultured 7 days under adherent culture conditions. A, Immunostaining for cardiac troponin T (cTnT) with DAPI nuclear staining in the single cardiomyocytes derived from each control and HCM iPSCs. B, Immunostaining for α-actinin with DAPI nuclear staining in the single cardiomyocytes derived from each control and HCM iPSCs. C, Cell surface areas of 798 to 823 randomly chosen cTnT-positive cardiomyocytes from each control (1 to 3) and HCM (1 to 3) group were measured at each time point. **$P<0.01$ vs control in the same time point (repeated-measures ANOVA and Mann–Whitney U test).HCM indicates hypertrophic cardiomyopathy; iPSC, induced pluripotent stem cell.

myofibrillar intersected each other within the single cardio-myocyte (Figure 7). There was no significant difference at 30 days between control and HCM iPSC-derived cardiomyo-cytes, but HCM iPSC-derived cardiomyocytes showed a higher prevalence of myofibrillar disarray than the control iPSC-derived cardiomyocytes at days 60 and 90 (Figure 6D). The α-actinin protein content did not differ between control and HCM iPSC-derived cardiomyocytes, whereas cTnT and ANP protein
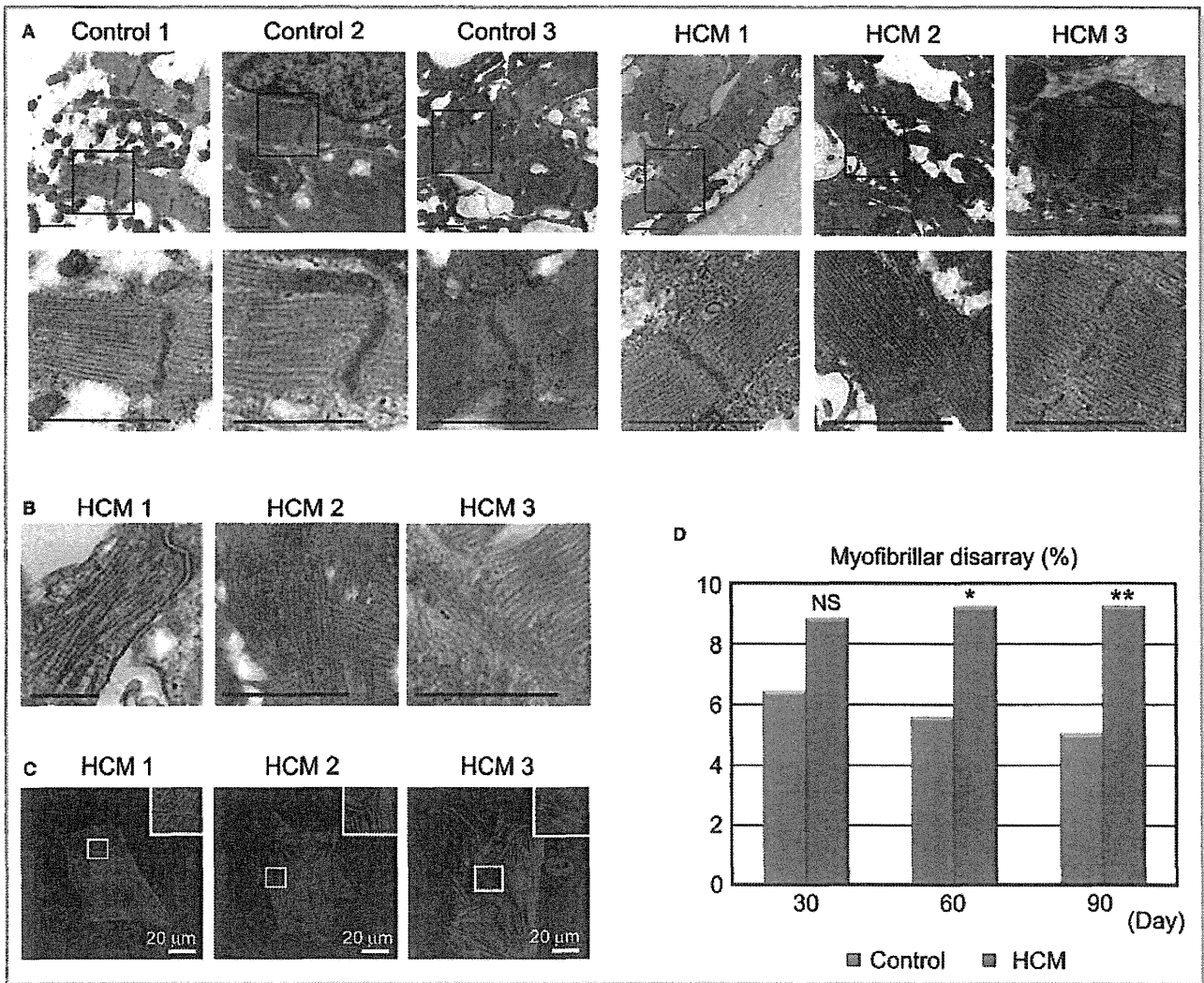
Figure 6. Structural characterization of iPSC-derived cardiomyocytes. A, Electron microscopic images showing well-organized striated myofibrils derived from beating EBs from control and HCM iPSCs at 60 days after differentiation. Scale bars, 1 μm. B, Electron microscopic images showing myofibrillar disarray derived from beating EBs from HCM iPSC at 60 days after differentiation. Scale bars, 1 μm. C, Immunostaining for cTnT in the single cardiomyocytes at 60 days derived from each HCM iPSC, showing myofibrillar disarray. D, The percentages of cardiomyocytes with myofibrillar disarray were assessed by cTnT immunostaining of the single cardiomyocytes. N=851 to 995. *$P<0.05$, **$P<0.01$ vs control in the same time point (χ^2 test). cTnT indicates cardiac troponin T; EBs, embryoid bodies; HCM, hypertrophic cardiomyopathy; iPSC, induced pluripotent stem cell.

levels were higher in the HCM iPSC-derived cardiomyocytes (Figure 8A through 8D). cMyBP-C protein level was lower in the HCM3-iPSC-derived cardiomyocytes (Figure 8E and 8F), suggesting cMyBP-C haploinsufficiency as observed in septal myectomy of HCM patients.[23,24]

ET-1 Unmasks Pathological Features in HCM iPSC-Derived Cardiomyocytes

To explore the mechanisms for deleterious pathogenesis in HCM, we examined the effect of several hypertrophic factors such as ET-1, angiotensin II, insulin-like growth factor 1, and phenylephrine on the iPSC-derived cardiomyocytes. The iPSC-derived cardiomyocytes were stimulated with each hypertrophic factor for 7 days (Figure 9A) and then analyzed for changes in the cell surface area and the incidence of myofibrillar disarray (Figure 9B through 9E). Some hypertrophic factors slightly, but significantly, increased cell surface area in control and HCM iPSC-derived cardiomyocytes (Figure 9B and 9C). We also analyzed the effect of the hypertrophic factors on myofibrillar disarray. Control iPSC-derived cardiomyocytes showed no change in the incidence of myofibrillar disarray following stimulation with the hypertrophic factors (Figure 9D), and
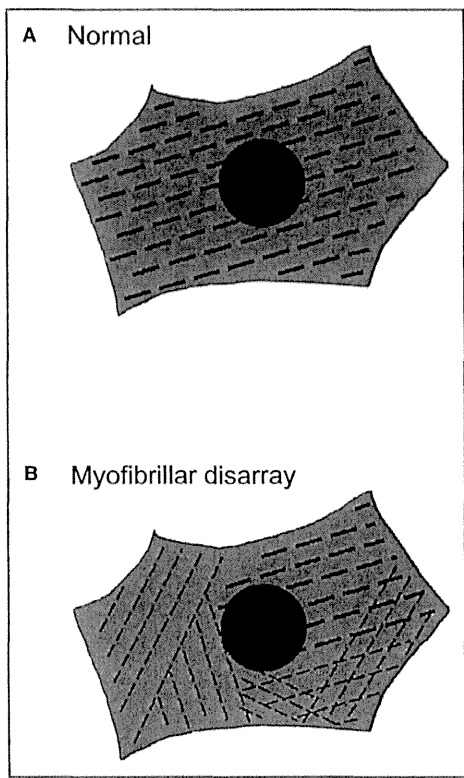
53

Figure 7. Schema of myofibrillar disarray in single induced pluripotent stem cell (iPSC)-derived cardiomyocytes. A, Cardiomyocyte with normal myofibrillar alignment. B, Cardiomyocyte with myofibrillar disarray.

Figure 8. Cardiac-specific protein expression in control and HCM iPSC-derived cardiomyocytes. A, Western blotting for α-actinin, cTnT, ANP, and GAPDH in control and HCM iPSC-derived beating EBs at 60 days after differentiation. B through D, Statistical analyses of α-actinin, cTnT, and ANP protein levels. N=4 to 6. *P<0.05 vs control (Mann–Whitney U test). E, Western blotting for cMyBP-C in control and HCM3 iPSC-derived beating EBs at 60 days after differentiation. F, Statistical analysis of cMyBP-C protein level. N=6. *P<0.05 vs control (Mann–Whitney U test). ANP indicates atrial natriuretic peptide; cMyBP-C, cardiac myosin-binding protein C; cTnT, cardiac troponin T; HCM, hypertrophic cardiomyopathy; iPSC, induced pluripotent stem cell; GAPDH, glyceraldehyde-3-phosphate dehydrogenase.

remarkably, ET-1 was the only hypertrophic factor to significantly increase the presence of myofibrillar disarray in the HCM iPSC-derived cardiomyocytes (Figure 9E). In addition, HCM iPSC-derived cardiomyocytes showed larger cell surface area and higher incidence of myofibrillar disarray than control iPSC-derived cardiomyocytes in each condition (Figure 10A and 10B). We also performed electron microscopic observation of beating EBs stimulated by ET-1, angiotensin II, insulin-like growth factor 1, or phenylephrine for 7 days. Only the HCM iPSC-derived cardiomyocytes exhibited myofibrillar disarray in the beating EBs after the ET-1 stimulation (Figure 11A). Although the ET-1 responsiveness was different between control and HCM iPSC-derived cardiomyocytes, the mRNA levels of endothelin receptor type A (*EDNRA*) and endothelin receptor type B (*EDNRB*) were not significantly different between control and HCM cells (Figure 11B and 11C).

To elucidate the fine regulation of ET-1 on the iPSC-derived cardiomyocytes, we treated the cells with different concentrations of ET-1. At baseline, HCM iPSC-derived cardiomyocytes have enlarged the cell surface area more than control cells. ET-1 increased the cell surface area in a concentration-dependent
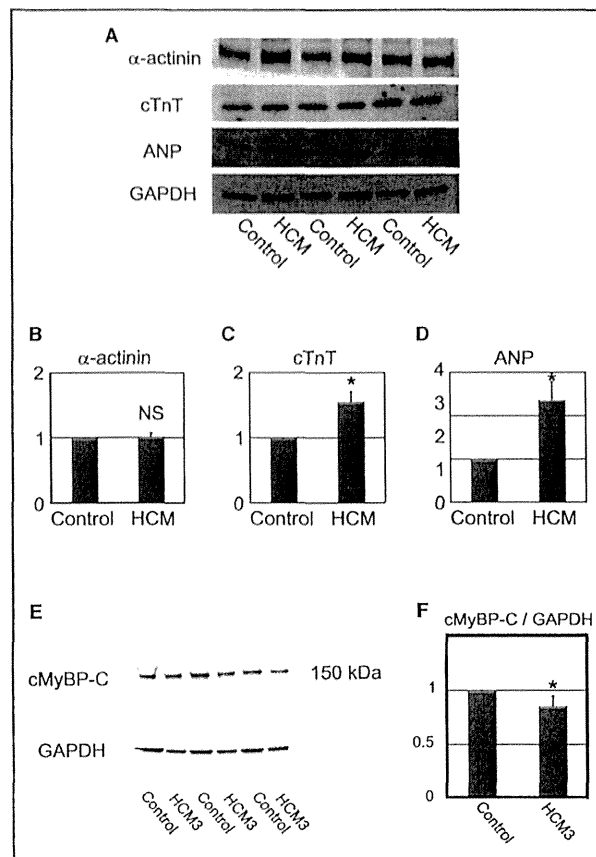
manner in both groups, and HCM iPSC-derived cardiomyocytes were more sensitive to ET-1 than were the control cells (Figure 12A). ET-1 had no significant effect on the incidence of myofibrillar disarray in the control iPSC-derived cardiomyocytes, while it increased the incidence of myofibrillar disarray in the HCM iPSC-derived cardiomyocytes in a concentration-dependent manner (Figure 12B). NFAT has been suggested to play a critical role in HCM pathogenesis.[25] The NFATc4 nuclear translocations were markedly increased on ET-1 treatment in the HCM iPSC-derived cardiomyocytes, compared with control cells (Figure 12C and 12D). We also examined other hypertrophic signaling such as extracellular signal-regulated kinase and c-Jun N-terminal kinase by using western blottings in the control

54